American Flame Research Committee
2022 Symposium
Greenville, South Carolina
September 12-14, 2022

Quantifying Flare Combustion Efficiency using an Imaging Fourier Transform Spectrometer

P. Lapeyre[1], R. B. Miguel[1], M. C. Nagorski[1], J-P Gagnon[2], M Chamberland[2], K. J. Daun[1]
[1]Department of Mechanical and Mechatronics Engineering, University of Waterloo
200 University Ave W, Waterloo ON, Canada
[2]Telops, Inc.. *100-2600 Avenue St Jean Baptiste, Québec QC, Canada*

Abstract

Mid-wavelength infrared (MWIR) hyperspectral imaging may be used to calculate the flare combustion efficiency from standoff measurements, without requiring any information about the fuel flow rate to the flare. Species column densities are found using a spectroscopic model, which is combined with a 2D velocity field from an optical flow model to obtain the mass flow rates of carbon-containing species within the plume. The technique is demonstrated by measuring the combustion efficiency of a steam-assisted flare at a petrochemical refinery.

Introduction

Climate change causes mass extinctions, mass disasters, mass migrations, and growing social inequity, all of which are rapidly intensifying as the planet warms. While much attention has focused on reducing carbon dioxide (CO_2) emissions, there is a growing awareness that hydrocarbon (HC) emissions from oil and gas processing significantly contribute to climate change due to the high global warming potential of these molecules. These emissions must be curtailed to avoid the worst outcomes of climate change. Flaring plays a crucial role in this effort. Under ideal operating conditions flares convert almost all the carbon in the HC molecules into CO_2, but real-world effects can significantly degrade the efficiency of this process. For example, under high crosswind-conditions, vortex shedding from the flare stacks may cause an aerodynamic fuel stripping mechanism [1], while steam- and air-assisted flaring, which is used to suppress soot formation, can also lead to excess HC emissions [2].

Measuring flare combustion efficiency through extractive gas sampling is challenging due to the difficulty of accessing the flare plume and the limited temporal and spatial resolution achievable by this technique. While some recent laboratory studies have successfully used whole plume measurements to gain key insights into factors affecting combustion efficiency of flares operating at steady-state [3, 4], these techniques cannot be deployed in the field; nor can they capture highly localized or transient effects typical of flares.

Accordingly, flare operators and equipment manufacturers urgently need diagnostics that can quantify flare combustion efficiency through optical standoff measurements. Mid-wavelength infrared hyperspectral (MWIR-HS) imaging using imaging Fourier transform spectrometers (IFTSs) appears well-suited to this purpose [5]. These instruments generate a hypercube of spectral intensity images, each at a different wavelength, from interferograms produced from a sequence of MWIR images generated over different optical path lengths modulated by the interferometer mirror position. The temperature and species concentration distribution along each pixel line-of-sight (LOS) through the plume is inferred from a spectroscopic model and then converted into a column density. In parallel, a 2D intensity-weighted velocity field may be derived from the broadband MWIR images. The column densities and velocity field are then combined to obtain the mass flow rates needed to calculate the overall combustion efficiency. Miguel et al. provide a detailed discussion of the measurement model, as well as several laboratory-scale and CFD proof-of-concept studies [6].

This paper demonstrates a proof-of-concept fenceline combustion efficiency measurement made on a flare at a petrochemical refinery. While the IFTS provides rich spectral data, a major challenge concerns artifacts in the hypercube introduced by turbulence-induced fluctuations in the spectral intensity field, as well as lens flare. The former issue can be mitigated by post-processing the interferogram, while the latter remains to be addressed. Nevertheless, the results highlight the promise of this technique, and its potential to reduce greenhouse gas emissions from flaring.

Flare Combustion Efficiency

Flare combustion efficiency is defined as the mass flow rate of the carbon affixed to CO_2 in the flare plume divided by the mass flow rate of carbon entering the flare stack as a gaseous hydrocarbon. Since the latter quantity may not be readily available, particularly for fenceline monitoring, it may instead be inferred from a mass balance of all carbon-containing species in the flare plume

$$\mathrm{CE} = \frac{\dot{m}_{\mathrm{C,CO_2}}}{\dot{m}_{\mathrm{C,fuel}}} \approx \frac{\dot{m}_{\mathrm{C,CO_2}}}{\sum \dot{m}_{\mathrm{C}}} \tag{1}$$

As shown in Fig. 1, the mass flow rate of the kth species in the plume is found by integrating the product of the corresponding species column density (kg/m^2) with the normal component of the 2D projected velocity along a control line that transects the plume in the image plane

$$\dot{m}_k = \int_{\Theta} \rho_k(\theta)\,\mathbf{u}(\theta)\cdot\hat{\mathbf{n}}\,d\theta \tag{2}$$

The mass flow rates may be adjusted by the atomic mass fractions of each molecule to obtain the mass flow rates of carbon. The pixel column density of the kth species for the LOS at a location θ along the control line is

$$\rho_k(\theta) = \frac{M_k p}{k_{\mathrm{B}} N_{\mathrm{A}}} \int_{\mathrm{LOS}(\theta)} \frac{\chi_k(s,\theta)}{T(s,\theta)}\,ds \tag{3}$$

where M_k is the molecular mass of the kth species, p is the atmospheric pressure, k_{B} is Boltzmann's constant, N_{A} is Avogadro's number, and $T(s,\theta)$ and $\chi_k(s,\theta)$ are the temperature and mole fraction of the kth species evaluated at a location s along the control line pixel LOS. The procedure for calculating the projected velocity field is described in the next section. In principle the denominator of Eq. (1) could include soot, although the contribution of soot to the overall carbon balance is usually negligible [7].

Spectroscopic Model

Species concentration and temperature profiles are inferred using a spectroscopic inversion algorithm. The spectral intensity at wavenumber η entering the camera aperture is defined by the radiative transfer equation (RTE) along each pixel line-of-sight

$$I_\eta = I_{\eta,\mathrm{bg}} \exp\left(-\int_0^L \kappa_\eta(s)\,ds\right) + \int_0^L \kappa_\eta(s)\,I_{\eta,\mathrm{b}}\left[T(s)\right]\exp\left(-\int_s^L \kappa_\eta(s')\,ds'\right)ds \tag{4}$$

where L is the length of line-of-sight from behind the plume to the camera aperture, $I_{\eta,\mathrm{bg}}$ is the background intensity, $I_{\eta,\mathrm{b}}$ is the blackbody intensity, and κ_η is the spectral absorption coefficient. The background intensity may be determined from a pixel outside of the flare plume, although its contribution to I_η is usually negligible compared to the emission term for pixels in the flare plume. For N_s participating species (e.g. CO_2, CO, H_2O, and HCs) the spectral absorption coefficient is given by

$$\kappa_\eta(s) = \sum_{k=1}^{N_s} \kappa_{\eta,k}\left[\chi_k(s), T(s)\right] \tag{5}$$

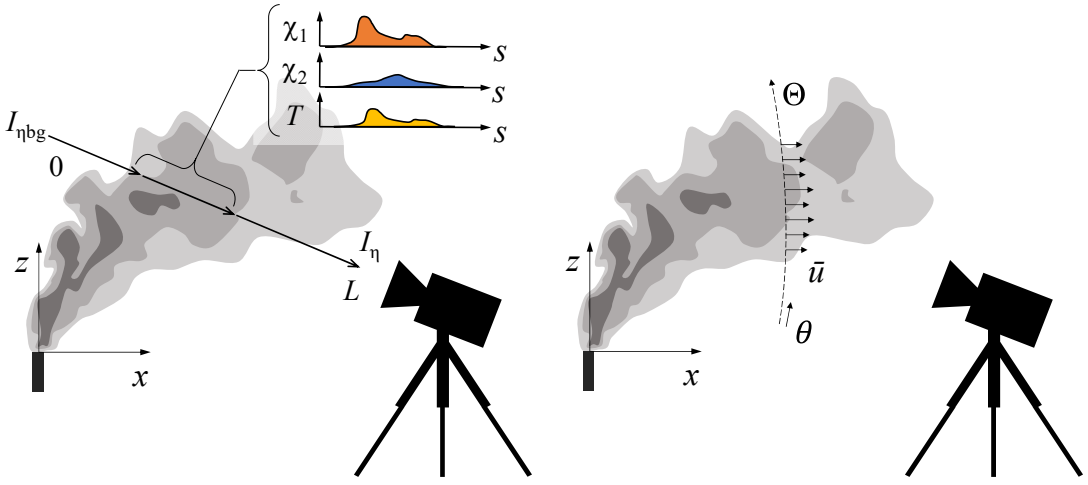

Figure 1: Schematic of a flare combustion efficiency measurement using an IFTS: (*a*) temperature and species concentration distributions are inferred from a spectroscopic model, Eq. (4); (*b*) these distributions are then used to derive column densities along a control line through Eq. (3), which is combined with a 2D intensity-weighted velocity map to obtain mass flow rates via Eq. (2).

The spectral absorption cross-sections of individual species may be found from a spectral line database (e.g. HITRAN [8]) or from experimentally-derived spectra. In the case of HITRAN-derived spectra, the absorption coefficients of common species are precomputed for given concentrations and temperatures, assuming air broadening. Further details about this procedure are provided by Miguel et al. [6].

Recovering the species mole fraction and temperature distributions from I_η is mathematically ill-posed. Accordingly, it is necessary to assign a parameterization to $\chi_k(s)$ and $T(s)$ along the pixel LOS; we assume Gaussian profiles, which are appropriate for free turbulent plumes:

$$\phi_k(s) = \phi_{k,\text{amb}} + \left(\phi_{k,\max} - \phi_{k,\text{amb}}\right)\exp\left(-\frac{s^2}{2\sigma_\phi^2}\right) \tag{6}$$

where $\phi = \chi_k$ or T, and σ_k is the characteristic length. The ambient concentrations and temperature may be derived from meteorological data, or determined by examining the spectra from a pixel outside of the flare plume, e.g., the flare stack. The plume thickness is assumed to be the same for all parameters and is estimated from the plume image, assuming that the plume is axisymmetric. Finally, the unknown parameters of Eq. (6) are inferred through weighted least-squares regression of the modeled spectrum to the measured spectrum.

Experimental Technique

Measurements were carried out on a steam-assist flare at a petrochemical refinery in Southwestern Ontario, shown in Fig. 2. Measurements were carried out on March 9th 2022, at approximately 4 PM Eastern Standard Time. The distance from the camera and flare stack was approximately 500 m. Hyperspectral imaging is done using a Telop MW HyperCam IFTS with a detection spectrum of 1900-3400 cm^{-1}, which includes vibrational-rotational bands of CO_2, H_2O, CO, and most HCs, and a maximum spectral resolution of 0.25 cm^{-1}. The focal plane array (FPA) is composed of 320×256 pixels. A 128×128 pixel subdomain of the FPA was used to image the flare, corresponding to a (22.4×22.4) m^2 area.

A pair of simultaneous images, each over a slightly different optical path, are captured as the interferometer mirror traverses through each of its measurement points; these images are optically combined to produce an image for the interferogram that must be deconvolved to obtain the spectrum. Specifically, the spectral intensity of pixel p and wavenumber η, S_p, is related to the measured interferogram counts, Y_p, by

$$Y_p\left[x(t)\right] = \int_0^{+\infty} \frac{1}{2}\left\{1+\cos\left[2\pi\eta x(t)\right]\right\} S_p(\eta,t)\,\mathrm{d}\eta \tag{7}$$

where x is the optical path difference (OPD) and t is the acquisition time. The spectral resolution, which is controlled by the maximum optical path difference (MOPD), was set to 4 cm^{-1}. With these parameters and an integration time of 100 μs per image, the imaging framerate was 747 Hz, which required 3.17 s to form a complete interferogram. Finally, the raw spectrum Y_p is transformed to obtain a raw intensity spectrum, S_p. The absolute intensity spectrum $I_p(\eta)$ is recovered through a two-point calibration measurement using blackbodies affixed to the camera.

Figure 2: Fenceline HS measurement of a steam-assist flare at a petrochemical refinery. The HS system, consisting of the camera, computer, power supply, and generator, was located approximately 500 m away from the flare.

A time-resolved 2D velocity field, $\mathbf{u} = [u, v]^T$, is derived from a set of successive raw interferometer images via the Lucas-Kanade optical flow algorithm [9]. The intensity of each image is first normalized and the mean pixel intensity field is subtracted to remove the stationary features. Optical flow is based on the hypothesis that any change in pixel brightness between successive images is due entirely to advection. Accordingly, pixel intensity becomes a conserved quantity and the velocity field is obtained by solving

$$\frac{DE}{DT} = \frac{\partial E}{\partial x}u + \frac{\partial E}{\partial y}v + \frac{\partial E}{\partial t} = 0 \tag{8}$$

where E is the modified broadband pixel intensity and the derivatives are found from finite difference approximations. The Lucas-Kanade algorithm adopts a weighted window scheme to filter the velocity field calculation, thereby suppressing noise amplification by the numerical derivative. Note that the optical flow algorithm works on the raw infrared images and not the absolute intensity spectrum found from deconvolving Eq. (7), since the former has a much higher framerate.

The measurement model assumed that the intensity field remains constant as the interferogram is assembled, which is not the case for flare plumes. Turbulent fluctuations, which occur over a much shorter time scale than the time needed for the mirror to traverse its entire OPD, manifest as "scene change artifacts" (SCAs) in the transformed intensity spectrum [10]. These perturbations are expressed in Eq. (7) through the time dependence of the intensity field, S_p. Following the hypothesis that the true intensity field is stationary but fluctuating, SCAs may be suppressed by using a high band pass filter to isolate the low frequency intensity variations, Figure 3 (*a*), and remove them from the measured interferogram to obtain a new filtered interferogram, Figure 3 (*b*).

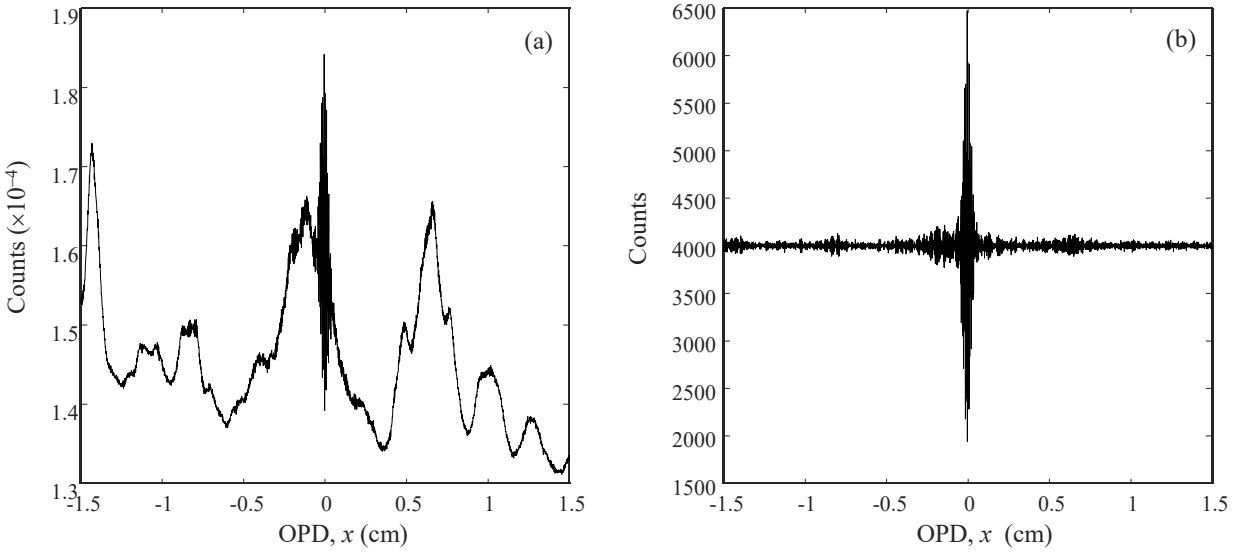

Figure 3: The raw interferograms (*a*) are contaminated by scene change artifacts caused by turbulent fluctuations in the flow field as the mirror traverses through its OPD. These can be removed through a filtering procedure (*b*).

Results

Figure 4 (*a*) shows the spectral intensity map for 2949 cm^{-1}, while Figures 4 (*b-d*) show the intensity spectra spectrum for pixels within the plume (*b*, *c*) and a pixel on the flare stack (*d*), along with absorption coefficients for H_2O, CO_2, and CO, all of which are expected to be in the flare plume. The intensity spectra indicate the presence of CO_2, H_2O, CO, and some HC in the plume, while broadband emission from the flare combustion zone and a combination of reflected incident and emitted intensity is also visible from the flare stack. The infrared intensity map also reveals lens flare artifacts, which extend diagonally from the flare. The lens flare artifact affects all of the broadband images used to construct the interferogram, and is therefore difficult to remove through image post-processing.

The feature between 2800-3000 cm^{-1} (3.3-3.6 μm) visible in Figures 4 (*b*) and (c) indicates the C-H stretching mode of a hydrocarbon. We assume that the HCs in the flare plume consist entirely of unburned fuel and that partially combusted/altered HCs are negligible. In the case of flares used to dispose of process gas for upstream oil and gas production this signal would likely be CH_4, but the absence of the R-branch lines at higher wavenumbers indicates the presence of a heavier hydrocarbon. Instead, the National Pollutant Release Inventory for this facility [11] suggests

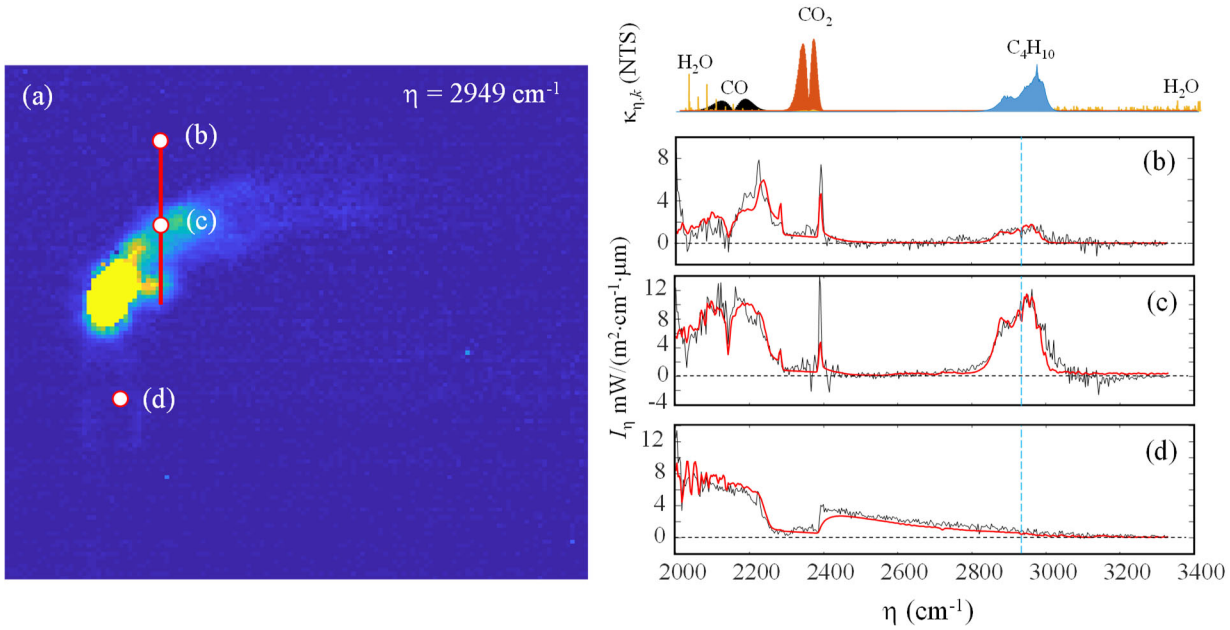

Figure 4: (*a*) Spectral intensity map of the flare, stack, and plume at 2949 cm^{-1}. The spectrum for the indicated pixels in the flare plume (*b*, *c*) reveal CO_2, H_2O, CO, and C_4H_{10}, while the spectrum of a pixel on the flare stack (*d*) is used to infer ambient CO_2 and H_2O, concentrations, as well as ambient temperature. The unscaled spectral absorption coefficients of the constituent are also plotted to aid in species identification. The red line in (*a*) indicates the control surface used to calculate the mass flow rates.

that the HC is butane, C_4H_{10}. Like many heavier hydrocarbons, line parameters for butane are not available in the HITRAN database. Instead, a comparison of the experimentally-derived molecular absorption cross-section [8, 12] and the IFTS emissions spectrum confirms that this emission feature likely corresponds to butane. This empirically-derived absorption spectrum is incorporated into the spectroscopic model.

The measured emission spectra from the plume, Figure 4 (*b*) and (*c*), reveals two CO_2 emission "spikes" at 2250 and 2400 cm^{-1}. This spectral pattern arises from emission from hot CO_2 in the flare plume that is absorbed by the ambient CO_2 between the flare plume and the camera, which is also responsible for the "gap" in the broadband reflected and emitted intensity from the flare stack in Figure 4 (*d*). The spikes in Figures 4 (*b*) and (*c*) correspond to hot lines at either end of the 001 fundamental CO_2 band that are not absorbed by the ambient CO_2. Given the long pathlength between the flare plume and the camera, it is crucial to account for the $^{13}C^{16}O_2$ isotopologue, which has a natural abundance of approximately 1% and a red-shifted absorption spectrum compared to that of the main $^{12}C^{16}O_2$ isotopologue.

In general, Figure 4 (*b-d*) shows that the modeled spectra are in excellent agreement with the measured spectra. The ambient CO_2 and H_2O concentration and temperature inferred from the spectrum in Figure 4 (*d*) are indicated in Table 1, and are consistent with other data sources.

Table 1: Ambient conditions during the hyperspectral measurement.

Parameter	Inferred from HS, Fig. 4 (*d*)	Expected value
CO_2	300 ppm	413 ppm[1]
H_2O	3170 ppm	3666 ppm (RH = 60%[2])
T_{amb} (K)	264 K	280 K[3] (280.3 K[2])

[1]Based on average atmospheric abundance
[2]Environment Canada, Simcoe Weather Station, 16:00 LMT March 9 2022
[3]Onboard thermocouple

The velocities found from the Lucas-Kanade algorithm are shown in Figure 5, while the column densities and temperature inferred from the spectra along the control surface are in Figure 6. The column densities show the expected patterns for the flare plume, although the two spikes in CO_2 concentrations likely correspond to lens flare features that are most pronounced at the wavelengths characteristic to CO_2 emission. The influence of these features on the overall mass flow rates is likely small due to the small magnitude of the corresponding normal velocity components. Column

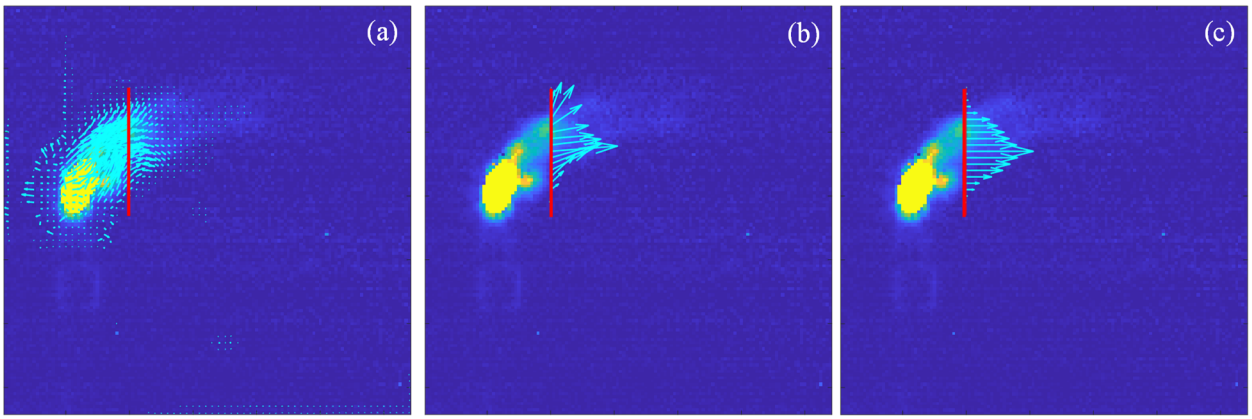

Figure 5: (a) 2D velocity field derived from the Lucas-Kanade algorithm; (b) along the control line; and (c) the component normal to the control line used to calculate mass flow rates.

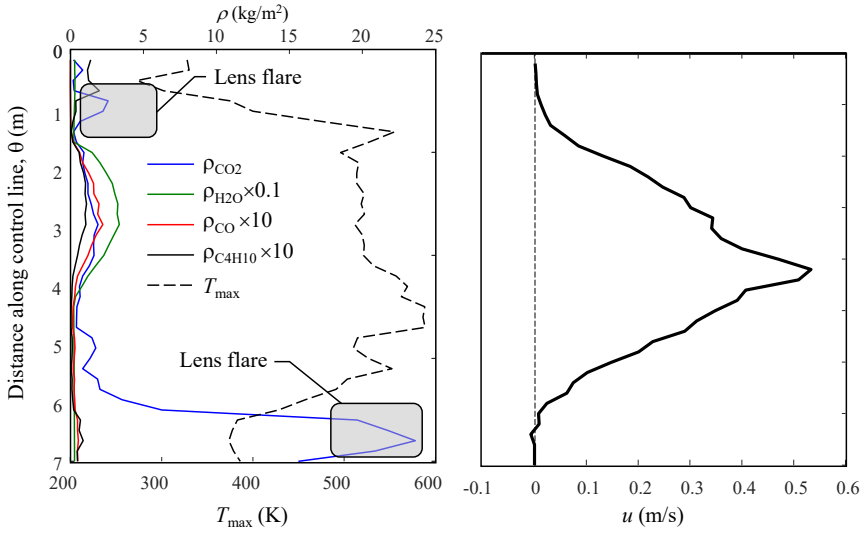

Figure 6: Velocity, temperature, and column density profiles along the control line. These parameters are substituted into Eq. (2) to obtain the mass flow rates. Lens flare artifacts are visible in the CO_2 spikes at 0.75 m and 6.5 m, but these are outside of the main plume velocity profile, and therefore do not impact the estimated mass flow rates.

densities and velocities are substituted into Eq. (2) to obtain the mass flow rates shown in Table 2. Finally, these mass flow rates are multiplied by their respective carbon mass ratios (CO_2: 12/44, CO: 12/28, C_4H_{10}: 48/58) and then substituted into Eq. (1) to obtain an overall flare combustion efficiency of 84%.

Table 2: CO_2, CO, and C_4H_{10} mass flow rates

Species	Mass flow rate, $\dot{m}_k$ [kg/s]	Mass flow rate of carbon, $\dot{m}_{k,C}$ [kg/s]
CO_2	1.449	0.395
CO	0.114	0.029
C_4H_{10}	0.058	0.048
CE		83.8%

Conclusions

This study presents a proof-of-concept fenceline flare combustion efficiency measurement using a MWIR HS camera. The mass flow rates needed for this calculation are found by combining species column densities inferred using a spectroscopic model with a 2D velocity field obtained using an optical flow algorithm. Crucially, this technique provides the capacity to infer flow rates and flare efficiency through fenceline measurements, without requiring any knowledge about the fuel flow rate supplied to the flare. This tool may be used by operators, flare equipment

manufacturers, and regulators to assess the combustion efficiency of flares *in situ* through standoff measurements. This information is crucial to understand and minimize the impact of petroleum processing on climate change.

Turbulence-induced SCAs and lens flare both impact the intensity spectrum, and therefore the inferred temperature and species column densities. While the impact of SCAs may be mitigated through filtering, flare artifacts are considerably more challenging to remove. Future work will focus on developing image processing techniques to remove lens flare, and experimental procedures for avoiding these features in the first place.

While upstream flaring is mainly used to dispose of natural gas, composed many of methane, as in the present case, the fuel used for downstream flaring often involves heavier HCs, sometimes of an undetermined composition. In this work the HC was identified with the aid of a database to which flare operators must report annual emissions estimates. However, it may be possible to infer the plume composition entirely through spectroscopic fingerprinting using a catalogue of known HC spectra [13]. Ongoing work is also focused on detecting and quantifying particulate matter emissions through HS emission spectroscopy, although the contribution of these emissions to the overall carbon balance is expected to be small.

Finally, previous studies carried out on synthetic data from a CFD-large eddy simulation of a flare in cross-flow reveal that the assumption of a Gaussian plume shape of equal width for each species is a key error source in the measurement model. Future work will explore other ways to parameterize these variables along each LOS.

Acknowledgments

This research was sponsored by NSERC's FlareNet (NETGP 479641-15). The authors are grateful to Caroline Turcotte and Defence Research and Development Canada for providing their Imaging Fourier Transform Spectrometer.

References

[1] M. R. Johnson, D. J. Wilson and L. W. Kostiuk, "A fuel stripping mechanism for wake-stabilized jet diffusion flames in crossflow," *Combust. Sci. Technol.,* vol. 169, pp. 155-174, 2001.

[2] M. Zamani, E. Abbasi-Atibeh, S. Mobaseri, A. H., A. Ahsan, J. S. Olfert and L. W. Kostiuk, "An experimental study on the carbon conversion efficiency and emission indices of air and stream co-flow diffusion jet flames," *Fuel,* vol. 287, p. 119534, 2021.

[3] D. J. Corbin and M. R. Johnson, "Detailed expressions and methodologies for measuring flare combustion efficiency, species emission rates, and associated uncertainties," *Ind. Eng. Chem. Res.,* vol. 53, pp. 19359-19369, 2014.

[4] E. Bourguignon, M. R. Johnson and L. W. Kostiuk, "The use of a closed-loop wind tunnel for measuring the combustion efficiency of flames in a cross flow," *Comb. Flame,* vol. 119, pp. 319-334, 1999.

[5] S. Savary, J.-P. Gagnon, K. Gross, P. Tremblay, M. Chamberland and V. Farley, "Standoff identification and quantification of flare emissions using infrared hyperspectral imaging," in *Proc. SPIE 8024, Advanced Environmental, Chemical, and Biological Sensing Technologies VIII, 80240T*, Orlando, 2011.

[6] R. B. Miguel, S. Talebi-Moghaddam, M. Zamani, C. Turcotte and K. J. Daun, "Assessing flare combustion efficiency using imaging Fourier transform spectroscopy," *J. Quant. Spectrosc. Rad. Trans.,* vol. 273, p. 107835, 2021.

[7] J. H. Pohl, J. Lee, R. Payne and B. A. Tichenor, "Combustion efficiency of flares," *Combust. Sci. Technol.,* vol. 50, pp. 217-231, 1986.

[8] I. E. Gordon, L. S. Rothman, R. J. H. R. Hargreaves, E. V. Karlovets, F. M. Skinner, E. K. Conway, C. Hill, R. V. Kochanov, Y. Tan, P. Wcisło, A. Finenko, K. Nelson, P. Bernath, M. Birk, V. Boudon, A. Campargue and K. Chance, "The HITRAN2020 molecular spectroscopic database," *J. Quant. Spectrosc. Radiat. Transf.,* vol. 277, p. 107949, 2022.

[9] B. D. Lucas and T. Kanade, "An iterative image registration technique with an application to stereo vision," in *International Joint Conference on Artificial Intelligence*, Vancouver BC, 1981.

[10] P. Tremblay, K. C. Gross, M. Chamberland, A. Villemaire and G. P. Perram, "Understanding and overcoming scene-change artifacts in imaging Fourier-transform spectroscopy of a turbulent jet engine exhaust," in *SPIE Optical Engineering and Applications*, San Diego CA, 2009.

[11] Government of Canada, "National Pollutant Release Inventory," [Online]. Available: https://www.canada.ca/en/services/environment/pollution-waste-management/national-pollutant-release-inventory.html. [Accessed 30 June 2022].

[12] S. W. Sharpe, T. J. Johnson, R. L. Sams, P. M. Chu, G. C. Rhoderick and P. A. Johnson, " "Gas-Phase Databases for Quantitative Infrared Spectroscopy", Applied Spectroscopy 58, 1452-1461 (2004)," *J. Quant. Spectrosc. Radiat. Trans.,* vol. 58, pp. 1452-1461, 2004.

[13] R. DeÍPapa Moreira Scafutto, C. Robertode Souza Filho, D. N. Riley and W. Jose de Oliveira, "Evaluation of thermal infrared hyperspectral imagery for the detection of onshore methane plumes: Significance for hydrocarbon exploration and monitoring," *Int J Appl Earth,* vol. 64, pp. 311-325, 2018.